I. X-RAY POWDER DIFFRACTION (XRD) PROFILE

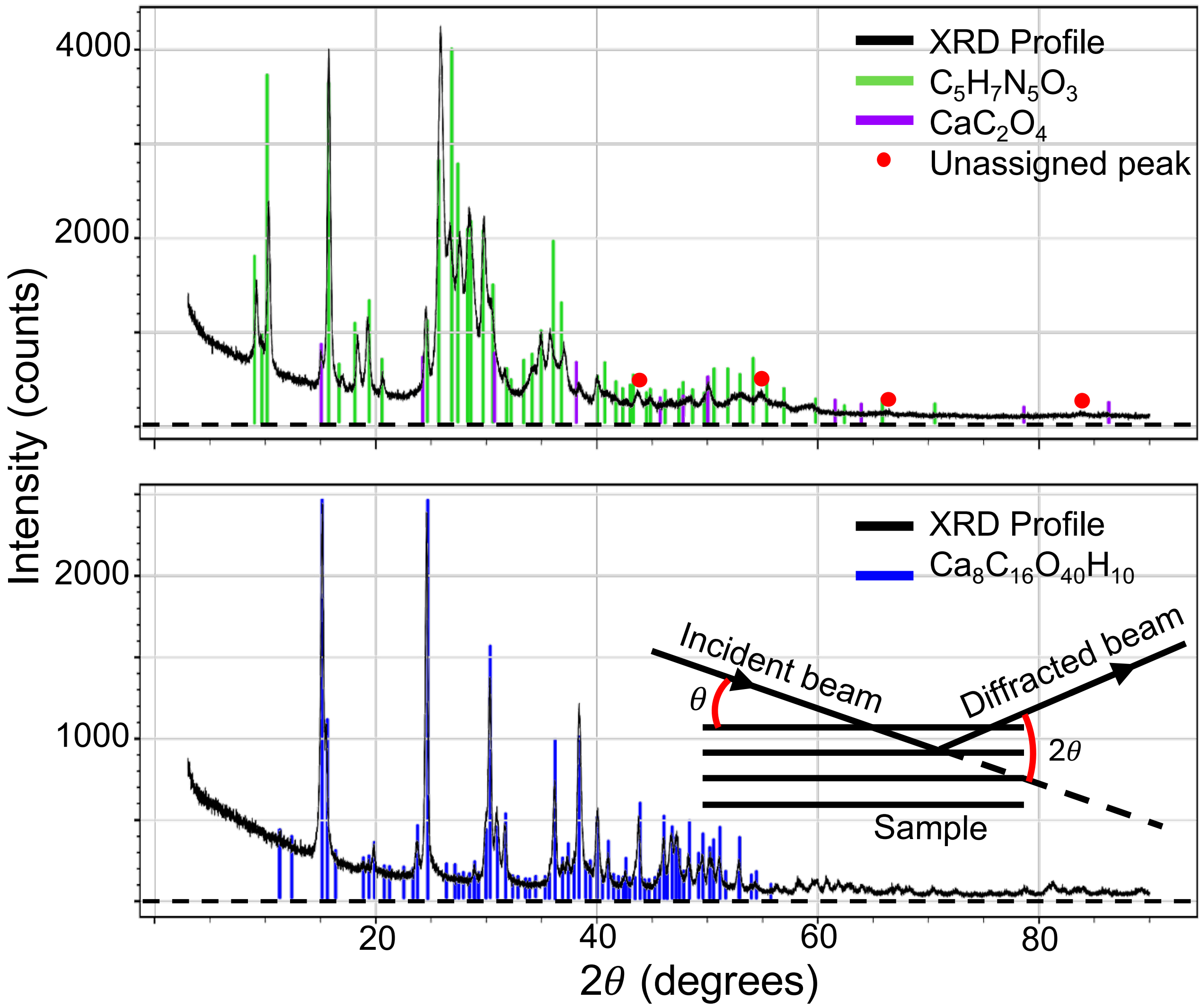

FIG. 1. X-ray powder diffraction (XRD) profile for AAU (A) and COM (B) and a simplified XRD schematic.

The X-ray powder diffraction (XRD) intensity respective to the two-theta diffraction angle for the AAU and COM stones is depicted in Fig. 1. A schematic of the two-theta diffraction angle with respect to the sample orientation is provided. For the AAU composition, $C_5H_7N_5O_3$ refers to ammonium urate while CaC_2O_4 refers to calcium oxalate. Peaks remain visible in the measured profile for which are unaccounted by these two constituent materials indicative of other trace composition materials. For the COM composition, high correspondence within the 10–55 degree window was achieved for $Ca_8C_{16}O_{40}H_{10}$ associated with Whewellite ($CaC_2O_4 \cdot H_2O$) or monoclinic calcium oxalate. One of the most prevalent kidney stone compositions is calcium oxalate monohydrate, with which we associate the correspondence of Whewellite. The detected microstructure observed through tomography reflects the expected structure of the asserted composition compared to examples in the literature indicating the XRD predicted material structure is likely valid. This figure supports the discussion regarding stone composition and prevalence in the Materials and Methods in addition to guiding the reference to the stone throughout the work. These measurements not bear influence on the analysis of the dynamics and damage evolution which are based purely on the observed and measured phenomena recorded using the multi-modal imaging technique demonstrated presently.

II. SEGMENTATION UNCERTAINTY VISUALIZATION

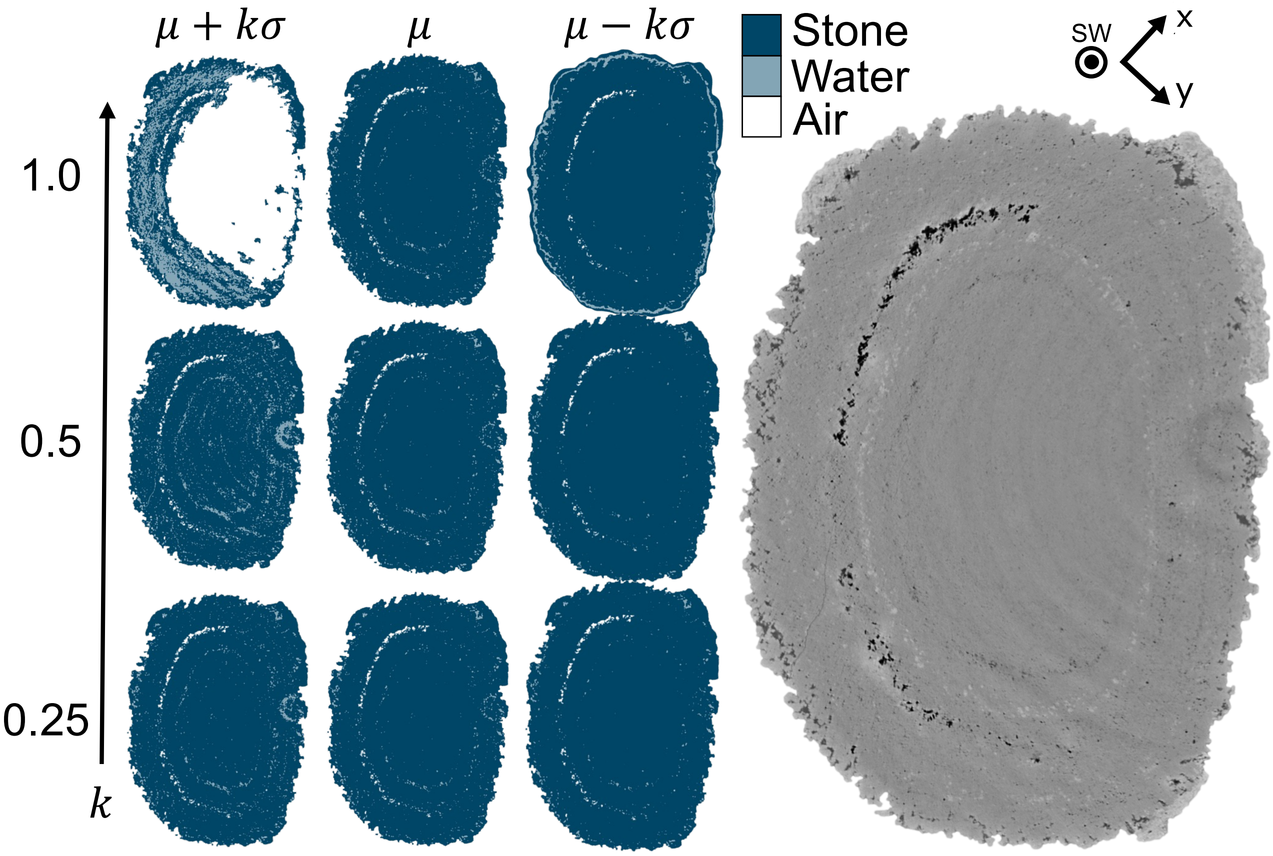

FIG. 2. Rendering of tri-class segmentation performance while varying Otsu thresholding parameters.

The effect of the uncertainty factor (k) on the tri-class semantic segmentation performance is depicted when adjusted between 1.0, 0.5, and 0.25 where μ and σ refer to the Otsu threshold value and noise within the foreground, respectively. The isolated foreground of the raw tomograph is depicted with the corresponding axes and shock wave propagation direction for clarity. The semantic segmentation section of the Materials and Methods specifies that the increasing the threshold ($+k\sigma$) provides a conservative solid material estimate, while decreasing the threshold value ($-k\sigma$) provides a liberal solid material estimate within the isolated foreground. The effect of this is demonstrated moving left to right across a consistent k value on the segmentation plot in Fig.2 and varies corresponding to the noise, or standard deviation, of the signal measured within the isolated foreground (σ). The adjustment of k (user-determined) is understood moving vertically up the k-axis for a constant standard deviation measurement. A k-value of 1.0 was rejected resulting from the deficient segmentation performance both within the stone and at edges. A k-value of 0.5 was rejected resulting from the over-influence of ring artifacts on the stone interior segmentation performance. A k-value of 0.25 was selected for effectively demonstrating reasonable conservative and liberal segmentation thresholding performance which could fall within skilled human detection performance. It is relevant to note that the Otsu-determined threshold value (μ) remained consistent throughout the procedure and that the value selected for k bears no influence on the mean threshold value.

III. ENERGY ESTIMATION

The potential energy, E_p, a single cavitation bubble at its maximum radius can transfer to the stone can be estimated by the following equation:

$$E_p = \frac{4\pi R_{\rm max}^3}{3}(p_{\rm atm} - p_v), \tag{1}$$

where $R_{\rm max}$ is the maximum bubble radius, $p_{\rm atm}$ is the pressure in the surrounding liquid environment (100 kPa), and p_v is the fluid vapour pressure at room temperature (2.3 kPa).

The parallel rays of the X-ray projection ensure that the radii of the bubbles are not distorted by depth of field. Averaging discernible bubble radii at maximum expansion yielded a average radius of 0.86 mm. We use this value along with atmospheric pressure to obtain an approximate of the potential energy of the cavitation transferable to the stone by a single bubble which is determined to be 0.26 mJ.

For approximately 50 visually distinguishable bubbles present near the stone surface, we estimate the potential energy of the surrounding bubbles to be approximately 0.013 J per each shock event. This estimate likely overstates the energy available for collapse-induced loading of the stone, as neighbouring bubble interactions reduce the effective pressure surrounding each bubble; nevertheless, it provides an initial approximation of the energy stored in the cavitation field.

IV. SUPPLEMENTARY VIDEO DESCRIPTIONS

1: High-speed optical imaging and High-speed X-ray phase-contrast imaging acquired for both stones
This video contains side-by-side synchronized videos demonstrating the optical and phase-contrast representations of each shock event for each stone. HSOI was captured on a Photron Nova camera. HSXPCI was captured on a Photron SA-Z camera. See *Experimental Details: High-speed imaging* in the Methods section for complete specifications of video parameters.

2: Background subtracted high-speed dynamic fracture video
This video demonstrates the capability of the Shimadzu HSXPCI to capture the fracture propagation in both stones. Each damage mechanism from the Article is indicated on the respective stones. SW 5, 6, and 7 are shown for AAU; while SW 1, 2, and 3 are shown for COM. All videos are played synchronously with overlain identification labels. See *Experimental Details: High-speed imaging* in the Methods section for complete specifications of video parameters.

3: Rotating 3D volume renderings for AAU treatment
High-resolution renderings of the sample are rotated and clipped to demonstrate external and internal damage over the course of the entire treatment. This directly compares the internal structure before and after treatment. Lower-resolution renderings are rotated to demonstrate the external damage for each individual SW. Prior to complete fragmentation, virtually no external damage can be identified because of the spallation dominant fracture mechanism.

4: Rotating 3D volume renderings for COM treatment
High-resolution renderings of the sample are rotated and clipped to demonstrate external and internal damage over the course of the entire treatment. This directly compares the internal structure before and after treatment. Lower-resolution renderings are rotated to demonstrate the external damage for each individual SW. Damage is externally evident for each SW and is clearly supported from the rendered volumes.